Three Dimensional Transonic Flow Computations Over a Projectile and at the Base Region

M. Malek Jafarian and M. Pasandideh Fard[1]

A three dimensional base flow code has been developed to predict the flow field around projectiles, including forebody and afterbody flows at transonic speeds. Full Navier-Stokes equations are solved using finite volume and Runge-Kutta time stepping techniques to compute the full flow field around a projectile including the base region at angle of attack. Flow field solutions have been obtained for a typical artillery projectile at Mach number, M=0.96 and 4 degree angle of attack. Details of the flow field on the boat-tailed afterbody and in the base region are presented. Surface pressure, base pressure and aerodynamic coefficients are computed and compared with experiments and the Sahu's computational results are achieved using thin layer approximation of governing equations.

INTRODUCTION

A major area of concern in shell design is the accurate prediction of the total aerodynamic drag. Both the range and terminal velocity of a projectile (two critical factors in shell design) are directly related to the total aerodynamic drag. The total drag for projectiles can be divided into three components: 1) pressure drag (excluding the base region), 2) viscous (skin friction) drag, and 3) base drag. At transonic speeds, base drag constitutes a major portion of the total drag. For a typical shell at $M = 0.9$, the approximate relative magnitudes of the aerodynamic drag components are around: 20% pressure drag, 30% viscous drag, and 50% base drag [1]. Further the critical aerodynamic behavior of projectiles occurs in the transonic speed regime, $0.9 \langle M \langle 1.1$, where the aerodynamic coefficients have been found to increase by as much as 100% because of the asymmetric shock pattern existing on the projectile and possible base region influence. Therefore, in order to predict the total drag for projectiles, computation of the full flowfield (including the base flow) must be made [2]. Base flows are an important subject of theoretical studies due to the determination role of the rear part of projectiles, missiles, or launchers in their flight capabilities. The problem of accurately predicting the aero-thermal fields in which they are embedded is still not satisfactorily solved by current theoretical methods.

1. *Department of Mechanical Engineering, Ferdowsi University, Mashhad 91775-1111, Iran*

Navier-Stokes solvers in combination with the algebraic turbulence model of Baldwin-Lomax have been applied to compute the base flows by Compton et al. [3] and Yang et al. [4]. Chuang and Chieng [5] also performed three higher-order turbulence models combined with Navier-Stokes equations to compute the supersonic flows behind a missile-type afterbody and two-dimensional two-stream flow behind a thick base. They solved the governing equations using an implicit total variation-diminishing algorithm to achieve high accurate results. Herrin and Dutton [6] experimentally investigated the near wake of a circular cylinder aligned with a uniform flow with Mach 2.5. Benay and Servel [7] performed a new two equation turbulence model ($\kappa - \sigma$) to predict the mean field and some fluctuating quantities in a supersonic base flow that was experimented by Herrin and Dutton. The turbulent structures in the highly compressible near-wake region of a cylindrical base, to which an axisymmetric sub-boundary-layer strip disturbance has been applied, were examined in detail using a planar Rayleigh/Mie scattering visualization technique by Bourdon and Dutton [8].

The first 3-D flow calculations performed by researchers did not include the base region flow and its effects on the upstream flow. Sahu et al. [1] developed an axisymmetric thin-layer Navier-Stokes base flow code to compute the entire projectile flow field including the base region using a unique flow field segmentation procedure. This code was used to compute base flow with and without base injection. Further Sahu

developed a three-dimensional time-marching, thin-layer, Navier-Stokes computational code in conjunction with a unique flow field over a projectile including the base region at angle of attack [2]. Because of less computer performance at that time and since the implicit solver was used, his computations were carried out in two pieces. The first one corresponded to the solution over the projectile with emphasis on the forebody solution and the other, containing the boat-tail corner and the base region. The objective of our effort is to extend the capability of the two-dimensional full Navier-Stokes, Runge-Kutta time stepping code into a three dimensional to include the upstream effect of the base flow and to compute the transonic flow over a projectile at angle of attack. The algorithm employed for the solution uses central differences with scalar artificial dissipations, implicit residual averaging and local time stepping. Time integration is performed by a four-stage Runge-Kutta scheme. The local values of the eddy viscosities are computed using the Baldwin-Lomax turbulence model. This capability including a unique O-type grid is used to predict the flow field over a 6 caliber secant-ogive-cylinder boat-tail projectile at M=0.96 and $\alpha = 4°$. The computed results obtained on a Pentium 600 MHZ computer are presented and compared to experimental data and computational results of Sahu [2]. A brief description of the governing equations is followed.

FORMULATION AND GOVERNING EQUATIONS

The non-dimensional unsteady Navier-Stocks equations in the conservation form and cylindrical coordinates can be written as:

$$\frac{\partial W}{\partial t} + \frac{1}{r}\frac{\partial (r\overline{E_r})}{\partial r} + \frac{1}{r}\frac{\partial \overline{E_\theta}}{\partial \theta} + \frac{\partial \overline{E_z}}{\partial z} + \overline{H} = 0 \qquad (1)$$

$$\overline{E_r} = E_r^i - E_r^v, \overline{E_\theta} = E_\theta^i - E_\theta^v, \overline{E_z} = E_z^i - E_z^v,$$

$$\overline{H} = H^i - H^v$$

Where the vectors $E_r^i, E_\theta^i,$ and E_z^i are the inviscid terms and $E_r^v, E_\theta^v,$ and E_z^v represent the viscous shear stress and heat flux terms. Also H^i and H^v are inviscid and viscous source terms respectively. Flux vectors are defined as follows:

$$w = \begin{bmatrix} \rho \\ \rho u_r \\ \rho u_\theta \\ \rho u_z \\ e \end{bmatrix}, E_j^i = \begin{bmatrix} \rho u_j \\ \rho u_r u_j + \delta_{jr} P \\ \rho u_\theta u_j + \delta_{j\theta} P \\ \rho u_z u_j + \delta_{jz} P \\ \rho u_j h \end{bmatrix},$$

$$E_j^v \begin{bmatrix} 0 \\ \tau_{jr} \\ \tau_{j\theta} \\ \tau_{jz} \\ u_r\tau_{jr}+u_\theta\tau_{j\theta}+u_z\tau_{jz}-q_j \end{bmatrix} H^i = \begin{bmatrix} 0 \\ -\frac{1}{r}(\rho u_\theta{}^2 + P) \\ \frac{1}{r}\rho u_r u_\theta \\ 0 \\ 0 \end{bmatrix},$$

$$H^v = \begin{bmatrix} 0 \\ -\frac{1}{r}\tau_{\theta\theta} \\ \frac{1}{r}\tau_{r\theta} \\ 0 \\ 0 \end{bmatrix}, j \rightarrow r, \theta, z$$

Where $u_r, u_\theta,$ and u_z are the cylindrical velocity components in the $r, \theta,$ and z directions, respectively; ρ is the density; P the pressure; and e the total energy.

Eq. (1) can be expressed in integral form as:

$$\frac{d}{dt}\int_\Omega w d\Omega + \int_{\partial\Omega} \overrightarrow{J}.\overrightarrow{n} dS + \int_\Omega \overline{H} d\Omega = 0 \qquad (2)$$

Where $\overrightarrow{J} = \overline{E_r}\vec{e}_r + \overline{E_\theta}\vec{e}_\theta + \overline{E_z}\vec{e}_z$ and $\overrightarrow{n}$ is the normal vector to the surface of element. $\overrightarrow{n}$ Consists of three components in $r, \theta,$ and z directions, and Ω is the volume of the element.

The numerical analogue of the integral Eq. (2) then reads:

$$\frac{dw}{dt} = \frac{1}{\Omega}(Q(w) + AD(w)) + H(w) \qquad (3)$$

Where $Q(w)$ denotes the convective flux given by an approximation of the surface integration in Eq. (2), $AD(w)$ is the artificially constructed dissipation operator and $H(w)$ is the source terms.

To include the viscous shear stress and heat flux terms, the velocity and temperature derivatives are estimated at the node points using central difference formulas in a computational space. The mesh transformation derivatives needed for the velocity and temperature derivatives are computed numerically.

NUMERICAL METHOD

As the discretization scheme leads to central difference approximation for the governing equations, additional artificial dissipative terms are necessary to damp out high-frequency oscillations. Here a blend of second and fourth differences of the flow variables as described in Reference [9] is used to form the dissipative operator $AD(w)$ (Scalar Dissipation Scheme). The second difference terms are used to prevent oscillations at shock waves, while the fourth difference terms are important for stability and convergence to a steady state [10].

The Scalar Dissipation Scheme has proved very effective in practice in numerous calculations of complex steady flows, and conditions under which it could be a total variation diminishing (TVD) scheme have been examined by Swanson and Turkel [11].

Since interest is usually focused on steady flow fields only, various techniques, like Local Time Stepping and Implicit Residual Averaging are used to accelerate convergence.

The local time step is taken to be:

$$\Delta t_{ijk} = \frac{CFL.\Omega_{ijk}}{\overline{\lambda}_r + \overline{\lambda}_\theta + \overline{\lambda}_z}$$

where the $\overline{\lambda}_r, \overline{\lambda}_\theta$ and $\overline{\lambda}_z$ are the average spectral radii of the Jacobian matrices in the r, θ and z directions. Implicit residual averaging is utilized in the following fashion:

$$\left(1 - \chi \delta_r^2\right) \left(1 - \chi \delta_\theta^2\right) \left(1 - \chi \delta_z^2\right) \overline{R}_{ijk} = R_{ijk}$$

where $\overline{R}_{ijk}$ is the averaged residual, and $\delta_r^2, \delta_\theta^2, \delta_z^2$ represent the second difference in r, θ and z directions, respectively. The constant χ may have typical values ranging from 0.25 to unity. The residual averaging requires three tridiagonal inversions, and is computationally quite costly. The residual averaging is applied to every stage of the Runge-Kutta scheme at the present work.

SOLVING GOVERNING EQUATIONS

The spatial discretization results in a system of ordinary differential equations in time, which is solved by an explicit Runge-Kutta time stepping scheme in the following manner:

$$w_{ijk}^{(0)} = w_{ijk}^n$$

$$w_{ijk}^{(q)} = w_{ijk}^{(0)} - \alpha_q \frac{\Delta t_{ijk}}{\Omega_{ijk}} \left(Q(w_{ijk})^{(q-1)} + AD(w_{ijk})^{(0)}\right.$$

$$\left. + \Omega.H(w_{ijk})^{(q-1)}\right) \quad q = 1 \text{ to } m \qquad (4)$$

$$w_{ijk}^{n+1} = w_{ijk}^{(m)}$$

with:

$$\alpha_2 = (1.2, 1), \alpha_3 = (\frac{3}{5}, \frac{3}{5}, 1), \alpha_4 = (\frac{1}{4}, \frac{1}{3}, \frac{1}{2}, 1),$$

$$\alpha_5 = (\frac{1}{4}, \frac{1}{6}, \frac{3}{8}, \frac{1}{2}, 1)$$

The bracketed superscripts in (4) refer to the stages of the Runge-Kutta scheme. $w_{ijk}^{(0)}$ is the value of w at the beginning of a time step and $w_{ijk}^{(q)}$ is the value after the execution of the q-th level of computation within that time step. However, in this work we generally used the four stage scheme.

INITIAL AND BOUNDARY CONDITIONS

The initial procedure is to use uniform free stream flow everywhere except $u_r = u_\theta = u_z = 0$ along the body surface. On the body surface, we have no slip boundary conditions. The pressure and density are extrapolated at the body surface from the first grid line above the body surface. Outer boundary is divided into two inlet and downstream parts. Constant free stream values are used for all variables at the inlet, whereas all variables at the downstream are obtained through extrapolation.

TURBULENCE MODELING

In the present calculations, two-layer algebraic eddy viscosity model of Baldwin-Lomax [12] is used. In their two-layer model, the inner region follows the Prandtl-Van Driest formulation. The outer formulation can be used in attached and separated boundary layers with minor modifications in wakes. The inner and outer layers viscosities are defined below:

$$\mu_i = \rho \left(Ky \left(1 - \exp\left(\frac{-y^+}{A^+}\right)\right)\right)^2 |\omega|,$$

$$\mu_o = \rho \kappa C_{cp} F_{wake} F_{kleb}(y)$$

The minimum of the two values results in the eddy viscosity at any point. Thus:

$$\mu_t = \min(\mu_i, \mu_o)$$

The details and constants are given in Reference [13].

MODEL GEOMETRY AND EXPERIMENT

The model used for the experimental and computational study presented here is an idealization of realistic artillery projectile geometry. The experimental model shown in Figure 1 consists of a three-caliber (1 caliber = maximum body diameter), sharp, secant-ogive nose, a two-caliber cylindrical midsection, and a one-caliber 7 deg conical afterbody or boattail. A similar model was used for the computational studies. The test conditions of 1 atm supply pressure and 320^{ok} supply temperature resulted in a Reynolds number of 4.5×10^6 based on
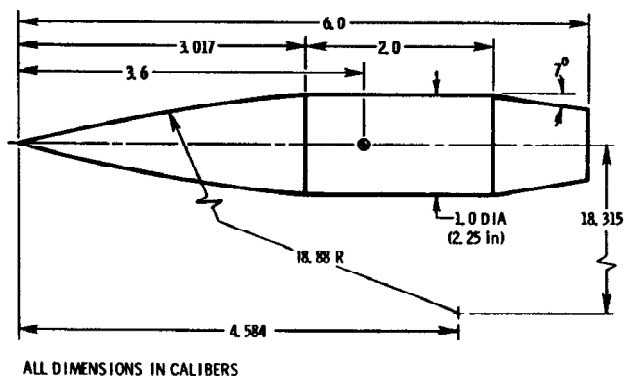

ALL DIMENSIONS IN CALIBERS

Figure 1. Model geometry

model length. The pressure data [14] were obtained with the non-spinning model.

COMPUTATIONAL GRID

The O-type grid used in this study was obtained by first solving the two-dimensional Poisson's equations for half of the symmetry plane of the cylinder (x-y plane), and then rotating this grid about the axis of the cylinder (Figure 2). This program allows arbitrary grid point clustering, thus enabling the grid points of the projectile shapes to be clustered in the vicinity of the body surface to resolve the viscous boundary layer. The computational mesh consisted of $154 \times 50 \times 20$ nodes in the axial, radial, and circumferential directions, respectively. The mesh size was set based on a computational study in which the mesh size was created progressively as long as further increase did not make considerable changes in the results. In this study, we considered three mesh sizes consisting $115 \times 40 \times 15$, $154 \times 50 \times 20$ and $192 \times 60 \times 25$ nodes. A mesh size of $115 \times 40 \times 15$ showed poor results compared to the experiment. When the mesh size was increased to $154 \times 50 \times 20$, the results were improved substantially. Further increase in the mesh size to $192 \times 60 \times 25$ made small improvements to the results but increased the CPU time dramatically. Therefore, the mesh size of $154 \times 50 \times 20$ was found to be the optimum size and was used in this paper. It should be mentioned that this mesh size is close to the one used by Sahu et al. [2]. The minimum normal spacings were on the order of $10^{-4} \times D$. An expanded view of the grid for the boat-tailed afterbody and the base region is shown in Figure 3. The outer flow field boundary was placed approximately 15 body diameters far away from the body surface. At this distance, the flowfield should be uniform and the imposed free stream boundary conditions should be valid.
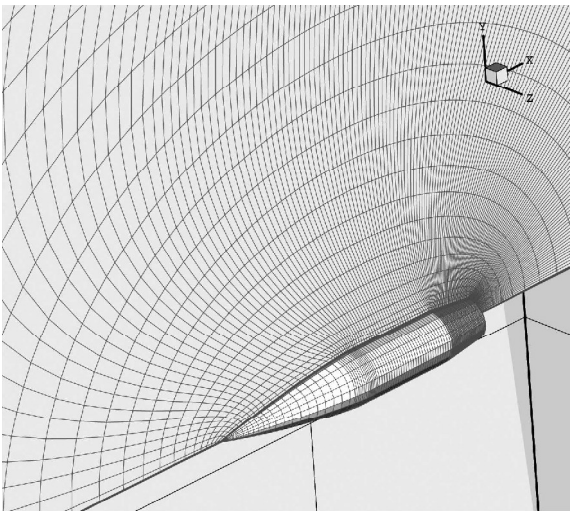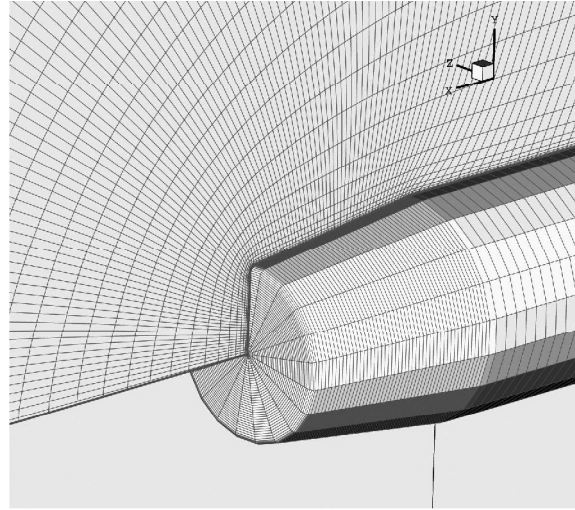

Figure 3. Grid over the boat-tail and at the base

RESULTS

The procedure is started by assuming uniform free-stream conditions for all grid points in the computational domain. By implementing boundary conditions the computation marches in time until a steady-state solution is reached. All the computed results are presented for $M = 0.96, \alpha = 4°$ and $CFL = 0.3$.

The streamlines in the base region for both the windward and the leeward planes are shown in Figure 4. The recirculatory flow in the base is evident. In addition, this figure shows the expected asymmetry in the recirculatory flow pattern in the windside and the leeside. The size of the separated bubble in the leeside is much larger than that on the windside.

Figures 5 and 6 are two and three-dimensional views, which respectively show the Mach and pressure contours over the projectile and in the base region for the windward and the leeward planes and on the surface of the projectile. The occurring expansion and
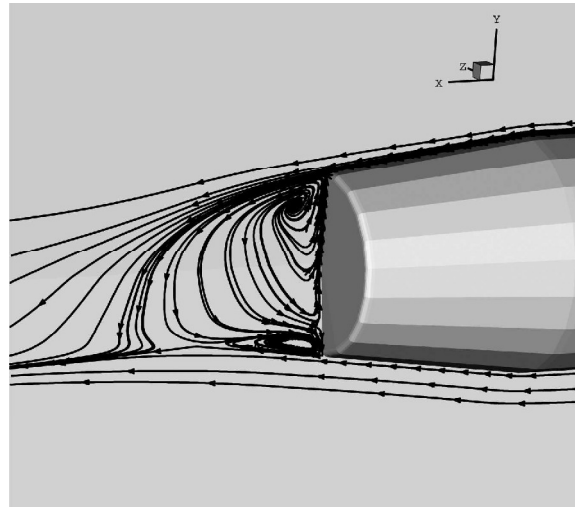

Figure 2. Grid over the projectile

Figure 4. Streamlines in windward and leeward planes at the base region ($M_\infty = 0.96$, $\alpha = 4°$)
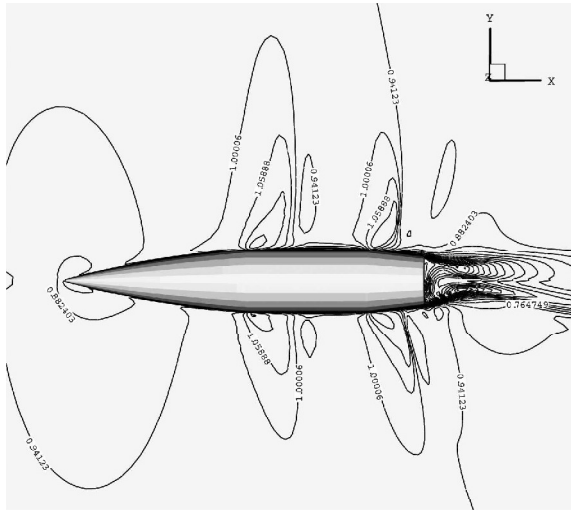
Figure 5. Mach Contours in Windward-Leeward plane and the base ($M_\infty = 0.96$, $\alpha = 4°$)
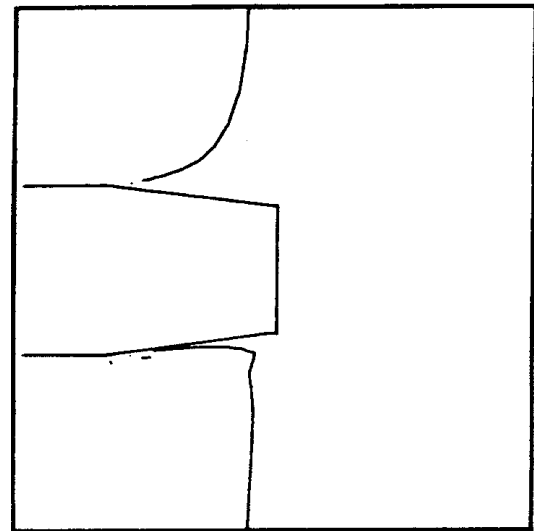

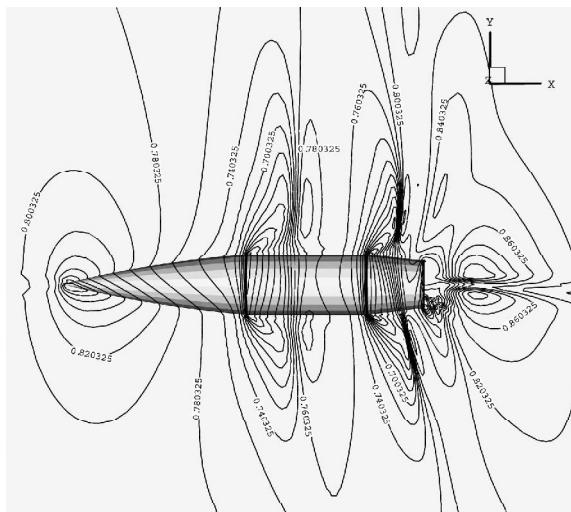**Figure 7.** Shock Locations on the Boat-tail $M_\infty = 0.96$, $\alpha = 4°$()

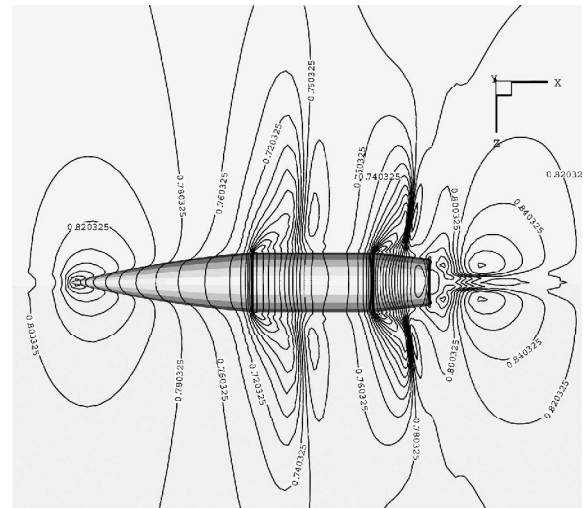**Figure 6.** Pressure contours in Windward-Leeward plane and the base ($M_\infty = 0.96$, $\alpha = 4°$)

Figure 8. Pressure contours in the perpendicular plane to Windward-Leeward surface ($M_\infty = 0.96$, $\alpha = 4°$)

shock wave at the boattail are shown in Figure 6. The expected asymmetry in the near wake flow filed is also clearly seen in this figure. The shock wave on the boat-tail in the windside is closer to the base than the one in the leeside.

The position of the shock wave is better shown in Figure 7. The shock location is based on looking at the Mach number component in the direction of the local pressure gradient. Where the Mach number goes through unity and then it is decreasing a shock is plotted. The shock structure is asymmetric. This is because of higher Mach number in the leeside than the windside for each longitudinal position. Figure 8 shows the pressure contours over the projectile and in the base region for the plane perpendicular to the windward and leeward planes. As we expected, the pattern of the flow is symmetric in this plane.

The surface pressure coefficients are shown as a function of the longitudinal position for both the windside and the leeside in Figures 9 and 10. They are compared with experiments and Sahu's results [2]. The agreement between the present computational results and experiments [14] is high. Also the present results are better than Sahu's. As shown in the pictures, the expansions and recompressions near the ogive-cylinder and cylinder boat-tail junctions are captured adequately. The computed surface pressures on the leeside are lower than those on the windside, whereas the reverse is true on the boattail. This is because the shock wave on the boat-tail in the windside is closer to the base than the one in the leeside. Similar trend is observed in experimental data. Comparison between the predictions, Sahu's results and experiments for the
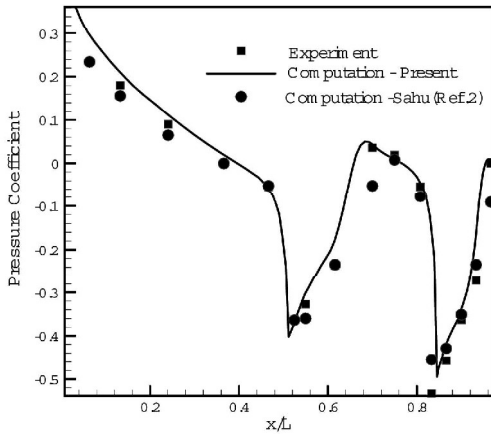
Figure 9. Longitudinal surface pressure in the Windward plane ($M_\infty = 0.96$, $\alpha = 4°$)
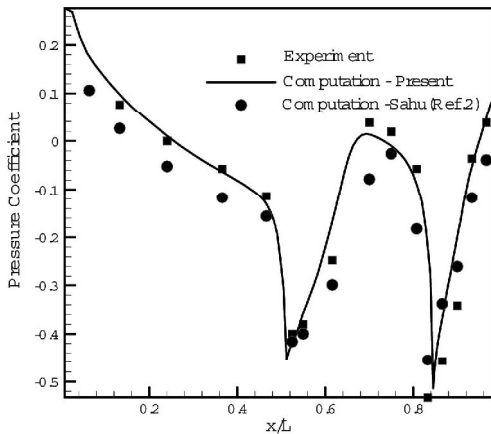

Figure 10. Longitudinal surface pressure in the Leeward plane ($M_\infty = 0.96$, $\alpha = 4°$)

Figure 11. Circumferential surface pressure distribution ($M_\infty = 0.96$, $\alpha = 4°$)

Figure 12. Circumferential surface pressure distribution ($M_\infty = 0.96$, $\alpha = 4°$)

Figure 13. Circumferential surface pressure distribution ($M_\infty = 0.96$, $\alpha = 4°$)

circumferential surface pressure distribution is seen in Figures 11-13 for longitudinal positions x/L=0.75, 0.865, 0.926 and 0.963 respectively. Figure 11 shows the results at x/L=0.75 (cylindrical portion) and x/L=0.865 (on the boat-tail). As seen in the figure, the trend of data in the present computation is predicted well and the agreement between the computations and experiments is generally very high. While this agreement is very good in the windside ($\theta = 0$), for the Sahu's results, it gets worse as the leeside ($\theta = 180$) is approached. Figures 12 and 13 illustrate the comparisons at x/L=0.926 and 0.963. As seen in this figures, both computations (present and Sahu's results) predict the trend of the data correctly. But our results are much better than Sahu's predictions. The position of x/L=0.963 is on the boat-tail just ahead of the base corner (Figure 13) where the influence of the base
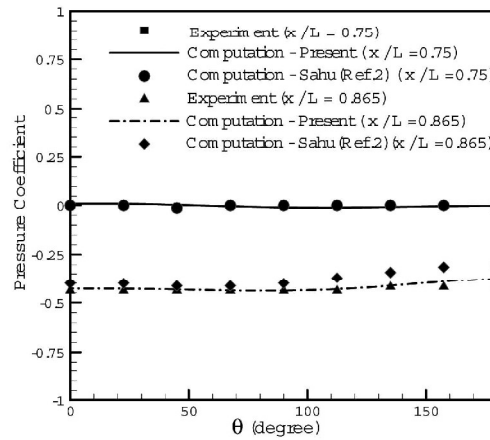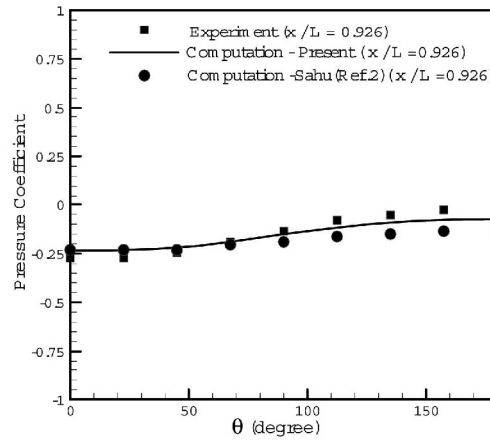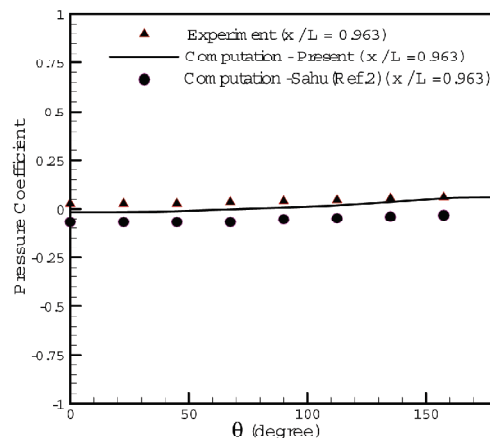
region flow is at its largest. Discrepancy between the Sahu's results and the experimental data is seen at all points in the circumferential direction at this stage. But this discrepancy is less in the present work.

Comparison between the computational and experimental data of circumferential pressure coefficients at 44% of the base radius from the centerline is shown in Figure 14. These results are under-predicted for both present and Sahu's works. This discrepancy is partly due to the data collection process [2] and/or because of the lack of adequate grid resolution on the boattail and turbulence modeling in the base region. In the wake region behind the projectile, the structure of the flow is not related to the wall or even the centerline. However, the algebraic turbulence model of Baldwin-Lomax predicts the eddy viscosity based on a combination of the distances from the base wall and the centerline. Thus, the velocities obtained in this work are larger than the experiments close to the wall. Consequently, the pressures achieved here are less than those in the experimental data. The trends of the present computational results for pressure are, although similar to the experiments, underpredicted. It must be mentioned that because we have a 3D domain, we are enforced to use simple turbulence models. However, still we can obtain desirable predictions for aerodynamics coefficients.

The final result desired from the flowfield calculations is the determination of the aerodynamic coefficients. The result to be presented here includes the normal force coefficient. This is obtained by integration of the pressure force acting on the projectile. Figure 15 shows normal force coefficient over the length of the projectile, which begins to rise rapidly on the ogive portion. The cylinder portion should produce no significant additional normal force as the present computation indicates a slight increase in the normal
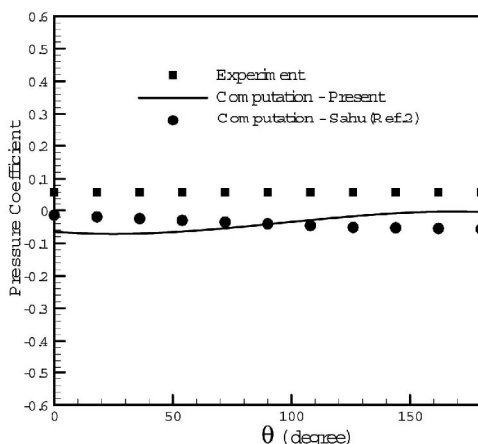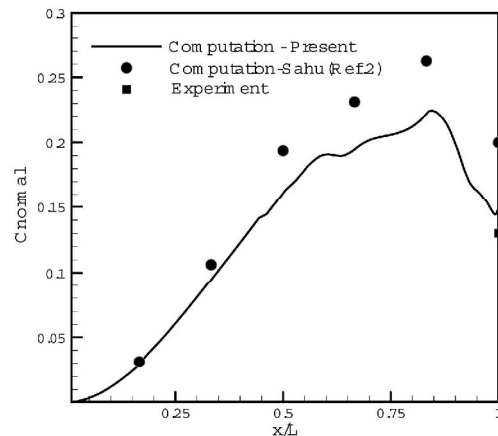

Figure 15. Development of normal force coefficient over the projectile ($M_\infty = 0.96$, $\alpha = 4°$)

force. A steep decrease is seen on the boat-tail resulting a very good agreement with the experimental data for the accumulated force coefficient. The accumulated normal force coefficient, indicated by the circle dark dots, has been over-estimated in the Sahu's results by about 30%. It is clear that the boattail has a dramatic effect on the aerodynamic coefficients. Thus, good resolution of the boattail flowfield is essential.

CONCLUSIONS

The elements of an unsteady, full Navier-Stokes base-flow code to compute the three-dimensional flow over a projectile at transonic speeds were described. Equations were solved using finite volume and Runge-Kutta time stepping techniques to compute the full flow field around the body including the base region at M=0.96 and $\alpha = 4°$. Computed results were compared with experimental data and also computational results of Sahu (unsteady, thin-layer, Navier-Stokes base-flow code).

Present results show the asymmetric wake in the base region and asymmetric shock located structure on the boattail upstream of the base corner. The agreement between the surface pressure distribution (longitudinal and circumferential), normal force coefficient and experimental data indicate that the present code is capable of predicting and simulating the complicated flow over the projectiles and the base region at transonic speeds very well.

ACKNOWLEDGMENT

Figure 14. Circumferential base pressure distribution ($M_\infty = 0.96$, $\alpha = 4°$)

REFERENCES

1. Sahu J. et al., "Navier-Stokes Computation of Pro-

jectile Base Flow with and without Mass Injection", *AIAA Journal*, **23**(9), (1985).

2. Sahu J., "hree-Dimensional Base-Flow Calculation for a Projectile at Transonic Velocity", *AIAA Journal*, **27**(2), (1989).

3. Compton W. B.,III, Abdol-Hamid K.S. and Abeyounis W.K., "Comparison of Algebraic Turbulence Models for Afterbody Flows with Jet Exhaust", *AIAA Journal*, **30**(11), PP 2716-2722(1992).

4. Yang A.S., Hsieh W.H. and Kuo K.K., "Theoretical Study of Supersonic Flow Separation over a Rearward Facing Step", *AIAA Paper*, 91-2116, (1991).

5. Chuang C.C. and Chieng C.C., "Supersonic Base-Flow Computation Using Higher-Order Closure Turbulence Models", *Journal of Spacecraft And Rockets*, **33**(3), (1996).

6. Herrin J.L. and Dutton J.C., "Supersonic Base Flow Experiments in the Near Wake of a Cylindrical Afterbody", *AIAA Journal*, **32**(1), (1994).

7. Benay R. and Servel P., "Two-Equation Turbulence Model: Application to a Supersonic Base flow", *AIAA Journal*, **39**(3), (2001).

8. Bourdon C.J. and Dutton J.C., "Altering Turbulence in Compressible Base Flow Using Axisymmetric

Sub-Boundary-Layer Disturbances", *AIAA Journal*, **40**(11), PP 2217-2224(8)(2002).

9. Jameson A. and Schmidt W., "Numerical Solution of the Euler Equations by Finite Volume Methods Using Runge-Kutta Time-Stepping Schemes", *AIAA Paper*, 81-1259, (1981).

10. Swanson R.C. and Turkel E., "On Central Difference and Upwind Scheme", *J. Comp. Phys.*, **101**, PP 297-306(1992).

11. Jameson A., "the Present Status, Challenges, and Future Developments in Computational Fluid Dynamics", Twelfth Australians Fluid Mechanics Conference, The University of Sydney, Australia, (1995).

12. Baldwin B.S. and Lomax H., "Thin-Layer Approximation and Algebraic Model for Separated Turbulent Flows", *AIAA Paper*, 78-257, (1987).

13. Srinivas K. and Rodi W., "Ein Programm Zur Berechnung Transsonischer Stromungen in Turbinengittern", FVV-VORHABEN NR. 337, (1987).

14. Kayser L.D. et al, "Surface Pressure Measurement on a Boattailed Projectile Shape at Transonic Speeds", ARBRL-MR-03161, (1982).